

Centrosome amplification mediates small extracellular vesicles secretion via lysosome disruption

4

Sophie D. Adams¹, Judit Csere¹, Gisela D'angelo², Edward P. Carter³, Teresa Arnanadis^{1,4}, Martin
8 Dodel¹, Hemant Kocher³, Richard Grose³, Graça Raposo², Faraz Mardakheh¹ and Susana A.
Godinho^{1,5,*}

12 ¹ Centre for Cancer Cell and Molecular Biology, Barts Cancer Institute, Queen Mary University of London,
Charterhouse Square, London EC1M 6BQ, UK

² Structure and Membrane Compartments, Institute Curie, Paris Sciences & Lettres Research University, Centre for
National de la Recherche Scientifique, UMR144, Paris, France

16 ³ Centre for Tumour Biology, Barts Cancer Institute, Queen Mary University of London, Charterhouse Square, London
EC1M 6BQ, UK

⁴ Current address: Department of Pathology, School of Medicine and Dentistry, Catholic University of Valencia, 46001,
Valencia, Spain.

20

24 ⁵ Lead Contact

* Correspondence should be addressed to S.A.G.: s.godinho@qmul.ac.uk

28 **Summary**

Bidirectional communication between cells and their surrounding environment is critical in both normal and pathological settings. Extracellular vesicles (EVs), which facilitate the horizontal transfer of molecules between cells, are recognized as an important constituent of cell-cell communication. In cancer, alterations in EV secretion contribute to the growth and metastasis of tumor cells. However, the mechanisms underlying these changes remain largely unknown. Here, we show that centrosome amplification is associated with and sufficient to promote small extracellular vesicle (sEV) secretion in pancreatic cancer cells. This is a direct result due of lysosomal dysfunction, caused by increased reactive oxygen species (ROS) downstream of extra centrosomes. Defects in lysosome function promotes multivesicular body fusion with the plasma membrane, thereby enhancing sEV secretion. Furthermore, we find that sEVs secreted in response to amplified centrosomes are functionally distinct and activate pancreatic stellate cells (PSCs). These activated PSCs promote the invasion of pancreatic cancer cells in heterotypic 3-D cultures. We propose that sEVs secreted by cancer cells with amplified centrosomes influence the bidirectional communication between the tumor cells and the surrounding stroma to promote malignancy.

44

48 **Keywords**

Centrosome amplification, exosomes, extracellular vesicles, ROS, lysosomes, PDAC, stellate cells, invasion

52

Introduction

A variety of human cancer types often exhibit defects in the structure and number of centrosomes, the main microtubule organizing centers in animal cells [1, 2]. Work in fly and mouse models has shown that centrosome abnormalities, in particular centrosome amplification, are not mere byproducts of tumorigenesis but rather play direct roles in promoting and accelerating tumor progression [3-6]. While the full extent by which centrosome abnormalities promote tumorigenesis is still unclear, centrosome amplification can directly promote aneuploidy and cell invasion, which play important roles in malignant progression [7-9]. Recently, we reported that centrosome amplification induces the secretion of several proteins with pro-invasive properties, e.g. interleukin-8, which induces invasive behavior in neighboring cells [10]. This altered secretion is partially due to a stress response that results from increased ROS downstream of centrosome amplification [10]. Thus, the presence of amplified centrosomes can also influence tumors in a non-cell autonomous manner, via protein secretion, suggesting a broader and more complex role for these abnormalities in cancer.

Secretion of cytokines, growth factors and extracellular vesicles (EVs) promote bidirectional communication between cancer cells and the tumor microenvironment (TME). This cross-talk impacts tumor initiation, progression and patient prognosis [11, 12]. EVs are membrane-bound vesicles containing proteins, lipids, DNA and RNA species (microRNA, mRNA and long non-coding RNAs) that can mediate the horizontal transfer of molecules between cells [13]. Their role in cell-cell communication is of particularly interesting due to their long-lasting effects and ability to influence distant tissues, e.g. during pre-metastatic niche formation [14]. Eukaryotic cells secrete two main types of EVs, microvesicles and exosomes, which differ in their size and biogenesis pathways.

Microvesicles (large EVs, μ EVs, ~100-1000 nm diameter) are formed through outward budding or “shedding” of the plasma membrane. In comparison, exosomes (small EVs, s EVs, ~30-150 nm diameter) are generated intracellularly as intraluminal vesicles (ILVs) within multivesicular bodies (MVBs), which are released upon the fusion of the MVBs with the plasma membrane [13]. Both types

80 of EVs are secreted by cancer cells and have been shown to play key roles in tumor progression, potentially via changes in their composition [15, 16].

Exosomes, a subtype of sEVs, are critical in shaping the TME [16]. This is particularly clear in the stromal
84 compartment, where cancer-derived exosomes can activate fibroblasts through transfer of molecules such as TGF- β [16-19]. Fibroblast activation leads to the deposition of extracellular matrix (ECM), tumor fibrosis and metastasis [20]. This is particularly important in pancreatic cancer, where activation
88 of the myofibroblast-like stellate cells, and consequent fibrosis, are the major contributors to the highly aggressive nature of these tumors and poor treatment efficacy [21-23]. While some exosomal components are known to contribute to fibroblast activation and recruitment (e.g. TGF- β and Lin28B) [19, 24], the pathways responsible for alterations in their packaging and secretion in cancer cells remain largely unknown.

92 Here, we show that the presence of extra centrosomes is sufficient to increase secretion of sEVs, but not large lEVs. Characterization of these sEVs by immunoelectron microscopy (IEM) and SILAC proteomic analyses suggests that they are of endocytic origin and thus enriched for exosomes.

96 Mechanistically, we found that disruption of lysosome function, as a consequence of increased ROS in cells with extra centrosomes, prevents efficient lysosome and MVB fusion, leading to sEV secretion. Furthermore, sEVs secreted by cancer cells with extra centrosomes are functionally distinct and can induce PSC activation. Consequently, pancreatic stellate cells (PSCs) pre-treated with sEVs from cancer
100 cells with extra centrosomes promote invasion of pancreatic ductal adenocarcinoma (PDAC) cells in heterotypic 3-D cultures. Our findings demonstrate that centrosome amplification promotes quantitative and qualitative changes in secreted sEVs that could influence communication between the tumor and the associated stroma to promote malignancy.

104

Results

108 **Centrosome amplification induces secretion of sEVs**

Our previous work demonstrated that centrosome amplification leads to proteomic changes in the secretome, including an increase in proteins associated with EVs, suggesting higher EV secretion in cells with amplified centrosomes [10]. To explore this further, we used an established
112 ultracentrifugation (UC) method [14] to crudely separate EVs according to their size: μ EVs and ν EVs, which we validated by nanoparticle tracking analyses (Figures S1A and S1B). To accurately measure secreted EV numbers, we used ImageStream flow cytometry to quantify fluorescently labelled EVs with the lipid dye BODIPY maleimide [25] and ensured that all serum was depleted for existing EVs by
116 UC (Figures S1C and S1D). We found that in the mammary epithelial cell line MCF10A where the secretome analysis was previously performed [10], induction of centrosome amplification, by transient overexpression of the Polo-like kinase 4 (PLK4) in response to doxycycline (DOX) [26], led to increased secretion of ν EVs, but not μ EVs (Figure S1E).

120 Due to the well-established role of ν EVs in activating fibroblasts, and its downstream effects on pancreatic cancer prognosis and treatment [16, 22], we decided to investigate if the presence of extra centrosomes would impact ν EVs secretion in pancreatic cancer. To do this, we quantified the number
124 of EVs and percentage of centrosome amplification in a panel of PDAC cell lines. We observed that cell lines with higher levels of centrosome amplification secreted increased numbers of EVs, in particular ν EVs, demonstrating a significant correlation between extra centrosomes and ν EV secretion (Figures 1A-1C and S1F). Furthermore, we confirmed that induction of centrosome amplification in two
128 pancreatic cell lines, PaTu-S and HPAF-II, is sufficient to increase secretion of ν EVs, but not μ EVs (Figures 1D and S1G). Additionally, depletion of SAS-6, a protein important for centrosome duplication, in cells exposed to DOX and PLK4 overexpression prevented both centrosome amplification and increased ν EV secretion, suggesting that ν EV secretion is indeed a consequence of centrosomal alterations (Figures
132 1D and S1G).

The sEVs fractions isolated by UC were enriched for several markers associated with exosomes, such as ALIX, CD63, TSG101 and CD81 [27], but not for general membrane markers, such as flotillin (Figure 1E). We further confirmed the presence of bona fide EVs in the sEVs fractions by EM and immunogold labeling using the SEV marker CD63 [28]. Consistent with increased sEV secretion, we found that the percentage of CD63^{+ve} EVs was higher in cells with extra centrosomes (+DOX) (Figure 1F). Moreover, these sEVs were slightly larger, assessed by EM and also nanoparticle tracking analyses, suggesting that qualitative changes might also occur in these EVs (Figures 1G and S1H). Altogether, our results demonstrate that centrosome amplification promotes sEV secretion.

Proteomic analyses of sEVs demonstrates their endocytic origin

To further understand the origin and composition of these sEVs, we performed stable isotope labelling by amino acids in cell culture (SILAC) proteomic analyses [29]. SILAC labelling with medium and heavy isotopes enables the exclusion of contaminant serum proteins, which would be unlabeled (equivalent of light labeling), and allows for simultaneous processing of purification steps to decrease sample-to-sample variability (Figure 2A). Because UC isolated fractions can contain contaminants, such as protein aggregates and cellular debris, we further purified the sEVs UC fraction using size exclusion chromatography (SEC) prior to proteomics analysis (Figure S2A). Commercially available qEV SEC columns designed to purify exosomes were used [30, 31] and sEVs were quantified by ImageStream, as before. As expected for these columns, sEVs collected from PaTu-S.iPLK4 cells (-/+ extra centrosomes) eluted in fractions 7-10, with the majority eluting in fractions 8 and 9 (Figure S2B). SILAC reverse and forward labelling was performed to conduct proteomic analyses of fractions 7, 8 and 9. Quantitative analyses of the proteomic data for each SEC fraction revealed that approximately 464 proteins were common to all fractions, and included known sEVs components such as ALIX, TSG101, CD81 and CD9 (Table S1). There were also proteins unique to each fraction suggesting that these sEVs are heterogeneous (Figure 2B). Comparison of our sEV proteomics data with the EV database Vesiclepedia [32] revealed that the majority of proteins in our datasets have been previously identified

160 in other EV studies, confirming the robustness of our purification protocol. Enrichment analyses of
common proteins present in both SILAC forward and reverse labeling experiments were performed to
identify common pathways (Tables S2 and S3). Importantly, the most significantly enriched categories
were associated with EV, sEV and linked to pathways unique for exosome biogenesis, such as recycling
164 endosome and endocytic vesicles (Figure 2D). Moreover, pathways linked to cell communication,
response to stress, pancreatic secretion and immune response were also enriched in our dataset
(Figure 2D), indicating that these sEV might have diverse functions.

168 To investigate if centrosome amplification impacts on sEV protein composition, we analyzed changes
in the ratio of proteins present in heavy and medium labelled sEV . Protein abundance was initially
median normalized to ensure that heavy and medium intensities in each sample were equivalent.
Interestingly, for proteins that a SILAC ratio could be calculated for, the ratio values did not
172 significantly change in any SEC fraction (Figure S2C and Table S4), suggesting protein composition is
largely unchanged in sEV secreted from cells with and without extra centrosomes. Overall, our SILAC
data demonstrate that while extra centrosomes do not induce a major change in the sEV s protein
composition, the content of these sEV s is consistent with an endocytic origin, indicating that this
176 fraction is likely enriched for exosomes.

Impaired lysosomal function in cells with extra centrosomes promotes sEV s secretion

MVBs are generally destined for degradation, by fusion with the lysosomal compartment, or are
180 trafficked to the cell periphery where they fuse with the plasma membrane, resulting in exosome
secretion [27, 33]. Lysosome dysfunction can shift the fate of MVBs targeted for degradation to fusion
with plasma membrane, leading to increased sEV s secretion (Figure 3A) [34-36]. We demonstrated
previously that centrosome amplification increases ROS [10], which can disrupt lysosomal function
184 [37, 38]. Therefore, we hypothesized that defective lysosomal degradation of MVBs could lead to
increased sEV s secretion in cells with amplified centrosomes (Figure 3A). To test this, we first assessed
whether induction of centrosome amplification led to increased ROS production in PDAC cell lines.

Indeed, induction of extra centrosomes increased ROS in both PaTu-S.iPLK4 and HPAF-II.iPLK4 cell
188 lines, as measured by the ratio of reduced versus oxidized glutathione, where a decrease indicates
higher ROS levels. Increased ROS can be abolished by treating cells with the ROS scavenger N-acetyl
cysteine (NAC), while hydrogen peroxide (H₂O₂) is sufficient to increase ROS levels in these cells
(Figures 3B and S3A). Using Magic Red fluorescence intensity to assess the function of the lysosomal
192 cathepsin B protease [39], we found that cells with extra centrosomes have compromised lysosomal
function. Treating cells with NAC prevented this defect, indicating that it was ROS dependent (Figures
3C, 3D and S3B). Furthermore, levels of LAMP1, a lysosomal marker, did not change in cells with extra
centrosomes or in response to increased ROS (Figures S3C-3E), suggesting that ROS specifically impair
196 lysosome function, consistent with their role in disrupting the integrity of lysosomal membranes [37].
Next, we analyzed sEVs secretion in response to ROS. These analyses revealed that whilst increased
ROS were sufficient to increase sEVs secretion in PDAC cells, preventing higher ROS production in cells
with amplified centrosomes, using NAC, abolished enhanced sEVs secretion (Figure 3E). These results
200 suggest that compromised lysosome function in cells with amplified centrosomes leads to sEVs
secretion. In agreement, inhibition of lysosome function with the vacuolar proton pump inhibitor
Bafilomycin A1, which impairs lysosome acidification [40], was sufficient to increase sEVs secretion
(Figures S3F-S3H) [41].
204
Next, we investigated if ROS could prevent fusion between MVBs and lysosomes, thereby promoting
MVB fusion with the plasma membrane and release of sEVs (Figure 3A). Using an antibody against
phospholipid lysobisphosphatidic acid (LBPA), a lipid enriched at the membranes of late endosomes
208 and MVBs [42], and lysotracker as a pH-based dye for functional lysosomes [43], we quantified the co-
localization of MVBs and lysosomes in the different conditions. Centrosome amplification decreased
the number of lysotracker-positive intracellular vesicles in a ROS-dependent manner but not LBPA-
positive intracellular vesicles, further supporting defective lysosomal function as consequence of
212 centrosome amplification (Figures 4A-4C). Strikingly, the percentage of co-localization between MVBs
and lysosomes was significantly decreased in cells with extra centrosomes. NAC treatment restored

lysosome function and MVB-lysosome co-localization in cells with extra centrosomes, while H₂O₂ was sufficient to decrease MVBs-lysosome co-localization (Figures 4A, 4B and 4D). Moreover, impairing
216 lysosome function with Bafilomycin A1 dramatically reduced MVB-lysosome co-localization (Figures S4A-S4D). Taken together, our data suggest that decreased MVB-lysosome fusion as a consequence of increased ROS, and subsequent lysosome dysfunction, promotes sEVs secretion in cells with supernumerary centrosomes.

220

sEVs secreted by cells with extra centrosomes activate pancreatic stellate cells to facilitate cancer cell invasion

Cancer-associated sEVs often carry altered cargoes, rendering them functionally distinct from sEVs
224 secreted by non-transformed cells [15, 16]. The exact causes of these changes, however, remain elusive. In PDAC, secreted sEVs may contribute to fibrosis through the activation of PSCs [44]. Thus, we investigated whether sEVs secreted by PDAC cells with extra centrosomes could promote the activation of PSCs. sEVs collected from PDAC cells +/- extra centrosomes (donor cells) were added to
228 PSCs (Figures 5A and 5B). Equal numbers of sEVs were added per condition to ensure that any differences observed were not due to the number of secreted sEVs. Activation of PSCs cells was assessed by immunofluorescence of alpha smooth muscle actin (α SMA). Increased expression and association of α SMA with stress fibers is a common feature of PSC activation towards a myofibroblast-
232 like phenotype [45] (Figure 5C). Interestingly, treatment of PSCs with sEVs secreted by PDAC cells with extra centrosomes led to activation of ~25-30% of the cell population (Figure 5D). It is important to note that by normalizing sEVs numbers, we are likely underestimating the differences between sEVs secreted by cells +/- centrosome amplification. As a positive control, PSCs were treated with TGF- β ,
236 a well-established activator of PSCs, known to lead to a strong activation phenotype (Figures S5A and S5B) [46]. To validate these results, we further purified the sEVs by SEC (Figures S2B and S5C) and tested the activation potential of the different isolated fractions. Not only were the sEVs harboring the potential to activate PSCs retained after SEC fractionation, but these sEVs associated mainly with

240 one fraction (SEC8 for PaTu-S.iPLK4 and SEC9 for HPAF-II.iPLK4) (Figure 5E), further supporting the
idea that secreted sEVs are indeed heterogeneous.

Fibroblast activation is a common feature of cancer and can promote cancer cell invasion through
244 various mechanisms including ECM remodeling and proteolysis [47]. To determine the functional
relevance of PSC activation by sEVs secreted by PDAC cells with amplified centrosomes, we
investigated their impact on PDAC cell invasion. To do so, we used 3-D heterotypic cultures of HPAF-
II cells that form spheroids in 3-D with PSCs (Figure 6A) [48]. In contrast to non-treated PSCs, or PSCs
248 pre-treated with sEVs from cells with normal centrosome numbers, PSCs pre-treated with sEVs
harvested from cancer cells with extra centrosomes significantly induced invasion (Figures 6B and 6C).
TGF- β pre-treated PSCs, used as positive control, showed higher invasion potential, consistent with
the stronger levels of PSC activation observed (Figures 6B, 6C and S5B). Confocal imaging of 3-D
252 spheroids composed of cancer cells expressing H₂B-RFP and PSCs expressing H₂B-GFP revealed that
activated PSCs lead the invasive front (Figure 6D). Our findings demonstrate that sEVs secreted by
PDAC cells with extra centrosomes are functionally different and can induce PSCs activation to
promote cancer invasion.

256

260

264

Discussion

268 In this study, we demonstrate that centrosome amplification induces secretion of sEVs that activate
PSCs promoting the invasion of cancer spheroids. Activated PSCs are major players in the development
of the pancreatic cancer stroma and associated fibrosis [21-23], suggesting a role for centrosome
amplification in shaping the pancreatic cancer TME. Our data support a model whereby elevated ROS
272 levels induced by extra centrosomes lead to loss of lysosomal function, favoring MVBs fusion with the
plasma membrane and sEVs secretion (Figure 7).

Lysosomes are signaling centers that integrate many cellular responses to changes in nutrients,
276 growth factors and stresses [49]. Fusion of lysosomes with autophagosomes is critical during
autophagy, a self-degradative process important for the removal of protein aggregates, damaged
organelles and intracellular pathogens [49]. Interestingly, centrosome amplification was recently
shown to disrupt autophagy, rendering these cells sensitive to autophagy inhibitors [50]. Whether
280 lysosome dysfunction is responsible for the autophagy defects observed in these cells is currently
unknown. However, it is reasonable to assume that ROS-mediated lysosomal dysregulation could have
a broader impact on the physiology of cells carrying centrosomal abnormalities.

284 sEVs secreted by cells with extra centrosomes exhibit many characteristics of exosomes: correct size
range (30-150nm) and proteomic profiling revealed an enrichment for proteins associated with
exosomes and exosome biogenesis. Sub-fractionation of secreted sEVs by SEC demonstrated not only
the existence of different sub-types of sEVs, as previously reported [51, 52], but that functional
288 differences between these different sEV populations also exist, as assessed by their ability to activate
stellate cells. How changes in sEVs composition occur and how these induce stellate cell activation,
however, remains elusive. One possibility is that changes in the sEV cargoes (proteins, RNA species)
could be involved in stellate cell activation. Indeed, whilst SILAC ratio values for most detected
292 proteins remained unchanged, we identified a number of proteins that were only identified in one
label, for which a SILAC ratio could not be calculated. Therefore, it is possible that some of these

proteins could play a role in PSC activation, but further studies will be required to assess if this is the case.

296

Alternatively, the presence or absence of specific proteins could influence sEV uptake and indirectly contribute to PSC activation. Cargo transfer by EVs can be mediated by delivery of surface proteins to membrane receptors, fusion with the plasma membrane, micropinocytosis, phagocytosis and

300

receptor-mediated endocytosis to deliver their content [53]. In addition, interaction between EVs and secreted proteins has been shown to modulate their uptake, highlighting the complex regulation of this process [54]. Tetraspanins, such as CD9, CD63 and CD81, have been shown to be involved in the interplay between adhesion molecules and integrins to promote sEV uptake [55]. The presence of

304

specific tetraspanins could also influence the specificity of target cells. For example, sEVs lacking the expression of the tetraspanin CD63 were found to be preferentially endocytosed by neurons [56].

Interestingly, we found that CD81 was the only protein absent specifically in the sEVs harvested from PDAC cells with amplified centrosomes that activate PSCs. Similarly, loss of CD81 has previously been reported in sEVs that are secreted upon induction of lysosome dysfunction [35]. Whilst the reason for this CD81 loss in response to lysosomal dysregulation is currently unknown, the striking similarity suggests a common response to lysosomal defects that could potentially modulate sEV uptake.

308

312

In summary, we describe a mechanism by which a stress response downstream of extra centrosomes culminates with the secretion of functionally different sEVs by diverging the fate of MVBs. Several cellular stresses have been shown to induce EV secretion, such as oxidative stress, hypoxia and radiation-induced cell stress [57]. Thus, it is possible that in response to multiple stressors, MVBs that

316

are normally targeted for lysosomal degradation play a role in the release sEVs carrying protective functions in order to maintain tissue homeostasis. Indeed, oxidative stress itself has been shown to induce changes in the mRNA content of exosomes secreted by mouse mast cells, which help to protect the surrounding cells by conferring resistance to subsequent oxidative insult [58]. Understanding how

320 stress communication protects cancer cells could allow us to exploit these mechanisms to prevent
cancer cell adaptation.

Acknowledgements

324 We are grateful to Judith Simon and all the members of the Godinho lab for comments or discussion
of the manuscript; Andrea Lafuente for providing the Dotplots used in Figure 2D; Hefin Rhys for
helping with ImageStream and Nanosight; Pedro Monteiro for advice on image analyzes. This work
was supported by a Cancer Research UK Centre Grant to Barts Cancer Institute (C355/A25137). E.P.C.
328 and R.G. were funded by Cancer Research UK (C10847/A27781). G.R. is supported by the French
Government (ANR) through the 20 Investments for the Future LABEX SIGNALIFE (ANR-11-LABX-0028-
01) and by the Fondation pour la Recherche Medicale (DEQ2011104211324). F.M. is supported by a
Medical Research Council (MRC) Career Development Award (MR/P009417/1) and a Barts Charity
332 grant (MGU0346). S.D.A. was supported by an MRC PhD studentship and J.C. supported by a Barry
Reed PhD studentship. S.A.G. is a fellow of the Lister Institute and is supported by the MRC
(MR/T000538/1).

336 Author Contributions

Conceptualization: S.D.A., S.A.G.; Methodology: S.D.A., T.A., G.D., E.P.C., R.G., G.R., F.M., S.A.G.;
Validation: S.D.A., J.C.; Formal Analysis: S.D.A., J.C., G.D., F.M., S.A.G.; Investigation: S.D.A., J.C., T.A.,
G.D., E.P.C., M.D.; Resources: H.K., R.G., G.R., F.M., S.A.G.; Data Curation: S.D.A., J.C., F.M.; Writing –
340 Original Draft: S.A.G.; Writing – Review & Editing: S.A.D., G.D., E.P.C., H.K., R.G., G.R, F.M., S.A.G.;
Visualization: S.A.D., J.C., G.D., E.P.C., S.A.G.; Supervision: H.K., G.R., F.M., S.A.G.; Project
Administration: S.A.G.; Funding Acquisition: S.A.G.

344 Declaration of Interests

The authors declare no competing interests.

Methods

Cell culture

348 Adherent cell lines were cultured at 37°C and 5% humidified CO₂. The pancreatic cancer cell lines PaTu-
8988t (PaTu-T; gift from Y. Wang, BCI-QMUL) PaTu-8988s (PaTu-S), Capan-1, PANC-1, CFPAC-1, HPAF-
II, MIA-PaCa-2 and DEC-hTERT (derived from normal pancreas) (gifts from H. Kocher, BCI-QMUL) were
grown in DMEM supplemented with 10% FBS and 1% penicillin and streptomycin. HPDE cells (derived
352 from normal pancreas) (gift from H. Kocher, BCI-QMUL) were grown in keratinocyte-SFM (1X) serum
free media +30µg/ml (BPE)+ 0.2ng/ml rEGF. The pancreatic stellate cell lines PS1 (gift from H. Kocher,
BCI-QMUL) [59] were grown in DMEM/F12 supplemented with 10% FBS and 1% penicillin and
streptomycin. 5 ng/ml of recombinant TGF-β (Peprotech) was used to treat PS1 cells for 72 hours.
356 Tetracycline-free FBS was used to grow cells expressing the PLK4 Tet-inducible construct. STR profiling
was performed for cell line authentication on the following lines: PaTu-S, PaTu-T, Capan-1, MIA-PaCa-
2, Panc-1 and PS1.

360 Chemicals

Chemicals and treatments were performed as follows: 2µg/ml Doxycycline hyclate (DOX; Sigma) for
48 hours, 100 µM H₂O₂ (Sigma) for 48 hours, 5 mM N-acetyl cysteine (NAC; Sigma) for 48 hours and
20 nM Bafilomycin A1 (Sigma) for 24 hours.

364

Lentiviral production and Infection

To generate lentivirus, HEK-293 cells were plated in antibiotic free medium. Transfection of the
appropriate lentiviral plasmid in combination with Gag-Pol (psPAX2, Addgene, 12260) and VSV-G (VSV-
368 G: pMD2.G, Addgene, 12259) was performed using lipofectamine 2000® (Thermo Fisher Scientific), as
per the manufacturer's specifications. The resultant lentivirus was harvested 24 hours and 48 hours
post infection, passed through a 0.4 µM syringe filter and stored in cryovials at -80°C. For infection,
the appropriate lentivirus was then mixed with 8 µg/ml polybrene before being added to the cells in

372 a dropwise fashion. Infection was repeated the following day and antibiotic selection started 24 hours after final infection.

Cells expressing the inducible PLK4 construct were generated as previously described [26]. Briefly, cells were initially infected with pLenti-CMV-TetR-Blast lentiviral vector (Addgene, 17492) and
376 selected using Blasticidin (10 µg/ml). Post-selection, cells were then infected with a lentiviral vector containing PLK4 cDNA which had been previously cloned into the pLenti-CMV/TO-Neo-Dest vector and selected using Geneticin (200 µg/ml) [26, 60]. Cells expressing the PLK4 transgene were then induced for 48 hours using 2 µg/ml of Doxycycline.

380 To generate H2B-RFP iPLK4 cells, lentivirus was produced by transfecting HEK-293 cells with LV-RFP (Addgene 26001), pMD2.G (Addgene, 12259) and µg pCMVDR8.2 (Addgene, 12263) using FuGENE (Promega, E2311), as per manufacturer's instructions. 24 hours later the medium was replaced and 48 hours post transfection the viral supernatant was collected, passed through a 0.4 µM syringe filter
384 and stored in cryovials at -80°C. Cells were transduced with the lentivirus as described above.

siRNA

siRNA transfection was performed in antibiotic free growth medium using Lipofectamine® RNAiMAX
388 as per the manufacturer's specifications. For SAS-6 knock down experiments siNegative control (siNegative, Qiagen, 1027310) and siSAS-6 (siSAS6 on-TARGET smart pool, Dharmacon, M-004158-02) were used. Per 6 well, 20 nM of siRNA was used for PaTu-S.iPLK4 cells and 50 nM for HPAF-II.iPLK4 cells as PaTu-S.iPLK4 cells were more sensitive to SAS-6 depletion and to prevent loss of centrioles
392 below control conditions. 24 hours post transfection, the cells were trypsinized and seeded onto coverslips for analysis by immunofluorescence or into 15 cm dishes for exosome harvest experiments 72 hours post transfection.

396

Immunofluorescence 2D

Cells plated on glass coverslips were treated for up to 48 hours with the appropriate drug treatments, before being washed twice in PBS and fixed in 4% Formaldehyde for 20 minutes at room temperature. For centrin2 staining, cells were fixed in ice-cold methanol for 10 minutes at -20°C. Following fixation, cells were permeabilized in 0.2% Triton X-100 in PBS for 5 minutes then blocked for 30 minutes in blocking buffer (PBS, 5% BSA, 0.1% Triton X-100). Cells were then incubated with primary antibody diluted in blocking solution for 1 hour. Cells were then washed with PBS and incubated with species-specific Alexa-conjugated secondary antibodies diluted in blocking buffer for 1 hour. Alexa Fluor 568 Phalloidin (1:250) was incubated in blocking solution for 1 hour. Cells were washed in PBS and DNA was stained with Hoechst 33342 diluted in PBS (1:5000) for 5 minutes. Finally, coverslips were mounted using ProLong™ Gold Antifade Mountant. Antibodies used included: Anti-centrin 2 N-17-R (Santa Cruz; 1:100), Anti α -tubulin DM1 α (Sigma-Aldrich; 1:1000), Anti LBPA 6C4 (Merck Millipore; 1:100), Anti LC3B (D11) XP® (Cell Signalling; 1:200), Anti α -SMA (Sigma-Aldrich; 1:300), Anti-Rabbit Alexa Flour 488 (Life Technologies; 1:1000), Anti-Rabbit Alexa Fluor 568 (Life Technologies 1:1000), Anti-Mouse Alexa Fluor 488 (Life Technologies 1:1000). Centrosome amplification was defined as the percentage of metaphase cells containing extra centrosomes (>4 centrioles per cell).

Images were acquired using an inverted Nikon microscope coupled with a spinning disk confocal head (Andor). Unless otherwise stated, imaging of cancer cells was performed using a 100x objective and imaging of stellate cells with a 40x objective. Images/projection images (from z-stacks) were subsequently generated and analyzed with Image J (National institute of Health, Bethesda, MD, USA) [61]. Where Z-stack images were required to analyze fluorescence intensity, Z-stack parameters were determined using the following equation: $Z_{min} = 1.4\lambda n / (NA_{obj})^2$. λ = the emission wavelength, n = refractive index of the immersion media, NA_{obj} = the numerical aperture of the objective. This equation calculates the ideal z stack step size to minimize overlap between each step of the stack. Sum intensity projection images were subsequently generated using Image J and fluorescence intensity was quantified using Image J. All conditions were quantified blindly.

424 **Extracellular Vesicle (EV) Isolation**

Cells were grown for 48 hours in medium supplemented with EV depleted FBS. Vesicle depletion in FBS was performed via ultracentrifugation at 100,000 x g at 4°C for 18 hours. Where induction of centrosome amplification was necessary, cells were treated with DOX for 48 hours, before cells were washed in PBS and subsequently cultured in EV depleted media. Where drug treatments were required, cells were treated for the duration of the EV harvest (48 hours post addition of EV depleted media). After 48 hours, conditioned medium was collected, and a final cell count was performed to ensure the final cell count remained the same between cell types and conditions.

432 Serial ultracentrifugation (UC). Extracellular vesicles were isolated from the conditioned media via serial ultracentrifugation steps at 4°C, similarly to [14]. Briefly, the cell culture medium was subjected to a low speed centrifugation of 500 x g for 10 minutes. The supernatant was then centrifuged at 12,000 x g for 20 minutes to pellet the large EVs (_LEVs), after removal of the supernatant the _LEVs were re-suspended in 500µl of PBS. The supernatant was then subjected to a high-speed ultracentrifugation at 100,000 x g for 70 minutes to pellet the smaller EVs (_SEVs). The pellet was then washed in PBS and a second high-speed ultracentrifugation was performed at 100,000 x g for 70 minutes (Figure S1A). The isolated _SEV pellet was then re-suspended in 500 µl of PBS.

440 Size exclusion chromatography (SEC). To further purify EVs isolated by serial ultracentrifugation, size exclusion chromatography (SEC) was performed using the qEV original izon science SEC columns (as per the manufacturer's instructions). Briefly, the SEC columns were equilibrated to room temperature and flushed with 5ml of buffer (PBS filtered twice through 0.22 µM filters) prior to use. 500 µl of concentrated exosomes (isolated by serial ultracentrifugation) was added to the top of the column and the eluted fractions were collected immediately in 500 µl volumes. The column was kept topped up with buffer throughout the experiment. Fractions 7-12 containing the eluted EVs were collected.

448

Extracellular Vesicle Quantification and Analysis

Amins ImageStream® Mark II Imaging Flow Cytometer (ImageStream). EV samples were analyzed by
452 ImageStream as previously described [25]. Briefly, samples were prepared in 50 µl volumes, labelled
with the fluorescent lipid dye BODIPY® FL Maleimide [BODIPY® FL N-(2-Aminoethyl) Maleimide]
(Thermo Fisher Scientific; 1:200) and incubated at room temperature in the dark 10 minutes prior to
analysis. Samples were then loaded onto the ImageStream and vesicles were acquired at a slow flow
456 rate with 60x magnification, a 488 nm excitation laser (BODIPY detection) and 765 nm laser (side
scatter). The “remove bead” function was turned off and the flow rate allowed to stabilize before
acquisitions. For acquisition, the storage gate was set to collect all events and the stopping gate set to
the vesicle population (low to mid BODIPY intensity and low side scatter). The stopping gate was set
460 to ensure that at least 20,000 objects were analyzed per acquisition. Three separate acquisitions were
collected per sample. Analysis was then performed using the IDEAS software. To quantify objects/ml,
a graph was generated plotting channel 02 fluorescence intensity (BODIPY) against channel 12 scatter
intensity (side scatter) and a vesicle gate was re-applied to select the population at the correct BODIPY
464 and side scatter intensities to be EVs (see Figure S1C). Where necessary the gate was adjusted using
the Image library to eliminate noise and artefacts from the vesicle population. The objects/ml statistic
was then used to quantify the number of objects/ml in the gated region. The average objects/ml was
calculated from three separate acquisitions from each sample.

468 Nanoparticle tracking analysis. Performed using a NanoSight NS300 with a high sensitivity camera and
a syringe pump. As previously described, isolated EVs were resuspended (UC) or eluted (SEC) in
Dulbecco’s PBS filtered twice through 0.22 µm filters. The NS300 chamber was flushed with 0.22 µm
filtered deionized water and then again with 500 µl of PBS (Dulbecco’s PBS filtered twice through 0.22
472 µm filters) to remove any particle matter. Using a 1 ml syringe 400 µl of EV sample was then flushed
through the chamber until vesicles were visible on the camera to allow the focus and gain settings to
be optimized. The sample was then injected into the flow cell at speed 50 and 3 recordings of 60
seconds each were acquired. Between samples filtered PBS was used again to flush the chamber

476 ensuring no residual particles remained. The data was then analyzed using the NTA 3.2 analysis software and averages of the three technical replicates were plotted per experiment.

Immunolabeling electron microscopy (IEM)

480 A drop (5 μ l) of sEVs (isolated by UC) suspended in PBS was deposited on formvar-carbon-coated electron microscopy grids for 20 min at room temperature, fixed with 2% paraformaldehyde in 0.2 M phosphate buffer (pH 7.4), for 20 min at room temperature, and post fixed with 1% glutaraldehyde in PBS for 5 min at room temperature. Grids containing sEV were then washed and then blocked for 5
484 min at room temperature in blocking buffer (PBS, 1% BSA). sEVs were then immunolabelled with a mouse anti-human CD63 primary antibody (Abcam ab23792) diluted in blocking solution for 1 hour at room temperature, washed with PBS, 0,1 % BSA, incubated with a rabbit antibody against mouse Fc fragment (Dako Agilent Z0412) in PBS 0,1% BSA for 20 min at room temperature. The preparations
488 were then immunogold labeled with protein-A gold-conjugates (10 nm; Cell Microscopy Center, Department of Cell Biology, Utrecht University). Grids were analyzed on a Tecnai Spirit G2 electron microscope (Thermo Fischer Scientific) and digital acquisitions were made with a 4k CCD camera (Quemesa, Soft Imaging System). Images were analysed with iTEM software (iTEM CE Olympus serie)
492 and data with Prism-GraphPad Prims software (v8) [62].

Western Blotting

Small extracellular vesicles harvested for protein extraction were isolated as previously described,
496 however following the final ultracentrifugation, the pellet was lysed immediately in RIPA buffer supplemented with protease inhibitors on ice. To facilitate further lysis, samples were probe sonicated on ice. Protein concentration was determined using the Bio-Rad Protein Assay. 10 μ g of protein was loaded per well. Samples were resuspended in Laemmli buffer, resolved using the NuPAGE[®] Bis-Tris
500 Electrophoresis System with NuPAGE[™] 10% Bis-Tris Protein Gels and transferred onto PDVF membranes. Antibodies used included: Anti TSG101 EPR7130(b) (Abcam; 1:1000), Anti CD63 (Abcam;

1:1000), Anti CD81 B-11 (Santa Cruz; 1:500), Anti ALIX 3A9 (Cell Signalling; 1:1000), Anti Flotillin-1 18
(Biosciences; 1:1000), HRP- anti rabbit secondary (GE Healthcare; 1:5000) and HRP- anti mouse
504 secondary (GE Healthcare; 1:5000). Western blots were developed on X-ray film using a SRX-101A
table top film processor.

Stable isotope labelling by amino acids in cell culture (SILAC)

508 SILAC based proteomic analysis of exosomes was performed as previously [63]. All SILAC amino acids
(heavy and medium) were purchased from Cambridge Isotopes. SILAC media and dialyzed serum were
purchased from Thermo Fisher Scientific. PaTu-S.iPLK4 cells with and without the induction of
centrosome amplification were grown for 6 passages in Dulbecco's modified Eagle's medium for SILAC
512 supplemented with 10% Gibco™ Dialyzed Fetal Bovine Serum (ultracentrifuged for 18 hours at
100,000 x g for EV depletion), 600 mg/L Proline and 100 mg/L of either heavy or medium Lysine and
Arginine amino acids (Lys⁸ and Arg¹⁰ for heavy, and Lys⁴ and Arg⁶ for medium, respectively). Labelled
cells were then plated at a density of 1x10⁶ cells in 40 T175 flasks per condition. 24 hours later flasks
516 were washed in PBS and 15 ml of fresh EV depleted medium supplemented with the correct amino
acids (heavy or medium) was added to the cells. 48 hours later, the conditioned medium was
harvested and samples heavy and medium labelled were pooled together (Figure 2A). EVs were then
isolated from the conditioned medium via ultracentrifugation and subsequent SEC as previously
520 described. The experiment was then repeated with the labelling reversed.

Mass spectrometry

Extracellular vesicles were lysed in 8 M Urea in 50 mM Ammonium bi-carbonate (ABC) (pH 8). Samples
524 were then sonicated using a Diagenode Bioruptor sonicator at 4°C. Samples were sonicated at high
power for 15 cycles of 30 seconds on and 30 seconds off. 10 mM DTT was added for 20 minutes at
room temperature followed by 55 mM Iodoacetamide incubated for 30 minutes in the dark. Protein
quantification was then performed as previously described. 15 µg of protein was then selected per

528 sample and Urea was diluted to 2 M final concentration with 50 mM ABC. Samples were then subjected to in-solution trypsin digestion overnight at 25°C. The digested peptides were then acidified and desalted via stagetipping [64]. Peptides were then dried by vacuum centrifugation and resuspended in 10 µl of buffer A* (2% ACN, 0.1% trifluoroacetic acid and 0.5% acetic acid).

532

LC-MS/MS analysis

Equivalent of ~1 µg of each digested SILAC mix was subjected to Liquid Chromatography coupled with tandem Mass Spectrometry (LC-MS/MS), using a Q-Exactive plus Orbitrap mass spectrometer coupled
536 with a nanoflow ultimate 3000 RSL nano HPLC platform (Thermo Fisher Scientific). Briefly, samples were resolved at a flow rate of 250 nL/min on an Easy-Spray 50 cm x 75 µm RSLC C18 column with 2 µm particle size (Thermo Fisher Scientific), using a 123 minutes gradient of 3% to 35% of buffer-B (0.1% formic acid in ACN) against buffer-A (0.1% formic acid in water), and the separated peptides
540 were infused into the mass spectrometer by electrospray. The spray voltage was set at 1.95 kV and the capillary temperature was set to 255 °C. The mass spectrometer was operated in data dependent positive mode, with 1 MS scan followed by 15 MS/MS scans (top 15 method). The scans were acquired in the mass analyzer at 375-1500 m/z range, with a resolution of 70,000 for the MS and 17,500 for the
544 MS/MS scans. Fragmented peaks were dynamically excluded for 30 seconds.

Proteomics data analysis

MaxQuant (version 1.6.3.3) software was used for database search and SILAC quantifications [65]. The
548 search was performed against a FASTA file of the Homo Sapiens, extracted from Uniprot.org (2016). A precursor mass tolerance of 4.5 ppm, and a fragment mass tolerance of 20 ppm was applied. Methionine oxidation and N-terminal acetylation were included as variable modifications whilst carbamidomethylation was applied as a fixed modification. Two trypsin miss-cleavages were allowed,
552 and the minimum peptide length was set to 7 amino acids. SILAC multiplicity was set to 3, with Lys4 and Arg6 selected as medium, and Lys8 and Arg10 as heavy labels. Minimum SILAC ratio count was

set at 1. All raw files were searched together, with the match between runs option enabled. All downstream data analysis was performed by Perseus (version 1.5.5.3) [52], using the MaxQuant ProteinGroups.txt output file. Briefly, normalized SILAC H/M intensities were converted to Log 2 scale. Reverse (decoy) hits, potential contaminants, and proteins identified only by modified peptides were filtered out. Ratio values were then median subtracted. Category enrichment analysis was performed using the Fisher exact test function within Perseus. Scatter plots of the SILAC ratio values were also generated by Perseus. All mass spectrometry raw files and search results reported in this paper have been deposited at the ProteomeXchange Consortium via the PRIDE [66], with the PRIDE accession number of PXD020984.

564 **Measuring cellular reactive oxygen species (ROS)**

Cellular ROS was measured through the detection glutathione in its reduced (GSH) and oxidized (GSSG) forms using the luminescence-based GSH/GSSG-Glo™ Assay (Promega, V6611). Briefly, the Promega GSH/GSSG-Glo™ Assay is a linked assay utilizing glutathione S-transferase and Luciferin-NT that generates a luminescent signal in response to levels of GSH present in the sample. The ratio of GSH to GSSG can then be calculated to give a read out of oxidative stress in the cells, where a decrease in the ratio indicates an increase in oxidative stress. All reactions and calculations were carried out as per the manufacturer's instructions. The final ratio of GSH/GSSG was normalized to protein content to control for any changes in cell number. Protein was quantified using the Pierce™ BCA Protein Assay Kit (Thermo Fisher Scientific, 23227) as per the manufacturer's instructions.

Magic Red assay

576 The Magic Red™ Cathepsin B kit (Bio-Rad, ICT937) was used to analyze the protease activity of Cathepsin B in lysosomes as a proxy to lysosome function. In the presence of functional cathepsin B, the Magic Red substrate is cleaved allowing the Cresyl violet fluorophore to fluoresce red upon excitation at 550-590 nm. Briefly, cells to be analyzed were plated on coverslips and the Magic Red

580 substrate (Magic Red stock was reconstituted in 50 μ l DMSO and diluted 1:10 in deionized water) was
added to the growth media (20 μ l was added per 300 μ l of growth media as per the manufacturer's
instructions) for the final hour of the experiment. Cells were then fixed in 4% Formaldehyde as
previously described. Cresyl Violet fluorescence was detected using an inverted Nikon microscope
584 coupled with a spinning disk confocal head (Andor). Z-stack images were acquired, and sum intensity
image projections were generated using Image J. Fluorescence intensity was then quantified per cell
with ImageJ [61]. All conditions were quantified blindly.

588 **Extracellular vesicle uptake by recipient cells**

Fluorescently labelled EVs were generated using the previously described ultracentrifugation protocol
with the following alteration: prior to the final PBS wash step, EVs were resuspended in 200 μ l of PBS
and fluorescently labelled with BODIPY (1:200). EVs were then incubated at room temperature for 5
592 minutes before being diluted in 31.5 ml of PBS. The final 100,000 x g ultracentrifugation step was then
performed, and the subsequent EV pellet resuspended in 200 μ l of PBS. The isolated EVs were then
added to the recipient cells that had been plated on glass coverslips 24 hours prior. 3 hours post
addition of EVs, coverslips were fixed in 4% formaldehyde and stained with Alexa Fluor 568 Phalloidin
596 (1:250) and Hoechst (1:5000) as previously described. Representative z-stack images were taken using
a spinning disk confocal microscope as previously described.

Extracellular vesicle-mediated PSC activation assay

600 PaTu-S.iPLK4 cells untreated or induced to have amplified centrosomes (48 hours 2 μ g/ml DOX
treatment) were cultured for 48 hours in vesicle depleted media before the conditioned media was
collected. EVs were then harvested from the conditioned media by ultracentrifugation alone, or in
combination with SEC as described previously. EV number was then quantified by ImageStream as
604 described above. 20 million EVs were then added to the culture medium of PS1 cells that had been
plated on glass coverslips at a density of 1×10^4 cells 24 hours prior. 48 hours later, a second dose of 20

million EVs was administered. 24 hours later cells were fixed and stained for α -SMA and DNA as described previously. Images were acquired using an inverted Nikon microscope coupled with a spinning disk confocal head (Andor) with a 40x objective. PS1 activation was quantified based on α -SMA organization, where the formation of α -SMA fibers was used as a measure of activation (maybe describe how the different categories were separated and we can reference the figure). Roughly 150 cells were quantified manually per condition. All conditions were quantified blindly.

612

3D co-culture spheroid invasion assay

Prior to spheroid generation, PS1 cells were either treated for 72 hours with sEVs (as described above), with 5ng/ml TGF- β or left untreated. 3D spheroid cancer cell/PS1 co-cultures were generated using a hanging drop spheroid model developed by Ed Carter and Richard Grose (BCI-QMUL), based on previous work [48]. Briefly, PS1 H2B-GFP (4.4×10^4 cells/ml) and HPAF-II.iPLK4-H2B-RFP cancer cells (2.2×10^4 cells/ml) were combined in a 0.24% methylcellulose solution (Sigma-Aldrich, M0512). Droplets containing 1000 cells were then plated on the underside of a 15 cm culture dish and left to form spheroids overnight at 37 °C. Spheroids were then collected and centrifuged at 100x g for 3 minutes before being re-suspended in gel mix solution. Gel mix solution consisted of 1.6 mg/ml Collagen I (Corning Rat Tail High Concentration) and 17.5 % Matrigel[®] Matrix Basement Membrane LDEV-free (Corning, 354234), prepared in PS1 culture medium and buffered to physiological pH with NaOH. Approximately 6 spheroids suspended in gel mix were added to a pre-coated well of a low attachment plate and left to solidify at 37 °C before PS1 culture medium was added on top. Spheroids were incubated for 3 days and images were taken by light microscopy. Percentage invasion was analyzed using Image J and calculated as a measure of the total invasive area relative to the central sphere. For confocal analyses, spheres were fixed in 4% formaldehyde prior to mounting for imaging on an LSM 880 Zeiss confocal microscope. All conditions were quantified blindly.

628

632 **Statistical Analysis**

Graphs and statistics were generated using Prism 8 (GraphPad Software) where results are presented as mean \pm standard deviation (SD) unless otherwise stated. Statistical analysis was performed using one-way ANOVA with either a Tukey's (parametric) or Kruskal-Wallis (non-parametric) post hoc test

636 unless otherwise stated. Significance is equal to * $p < 0.05$, ** $p < 0.01$, *** $p < 0.001$ and **** $P < 0.0001$.

640

644

648

652

656

Figure legends

Figure 1. Centrosome amplification promotes the secretion of sEVs in PDAC cells.

660 (A) Representative confocal images of mitotic cells with normal and amplified centrosomes. Cells were stained for α -tubulin (magenta), centrin2 (green) and DNA (cyan). Scale bar, 10 μ m. (B) Quantification of sEVs and lEVs secreted by PDAC cell lines. Average of the percentage of centrosome amplification (CA) per cell line is highlighted in orange. (C) Linear regression of the data presented in B and

664 Spearman correlation coefficients for sEVs and lEVs. (D) Quantification of secreted sEVs and lEVs in Patu-S.iPLK4 and HPAF-II.iPLK4 cell lines upon induction of centrosome amplification (+DOX), before and after depletion of Sas-6 by siRNA. Average percentage of centrosome amplification (CA) per condition is highlighted in orange. (E) Western blot analyses of proteins associated with sEVs in

668 extracts from cells and sEVs collected by UC. (F) Top: Representative images of IEM of sEVs collected from HPAF.iPLK4 cells. Dark beads represent immunogold labelling with anti-CD63. Scale bar, 200 nm. Bottom: Quantification of the percentage of positive CD63 sEVs. (G) Quantification of sEVs diameter by cry-EM. Patu-S.iPLK4 sEVs $n_{(-DOX)}=232$ and $n_{(+DOX)}=216$; HPAF-II.iPLK4 $n_{(-DOX)}=541$ and $n_{(+DOX)}=493$. For

672 all graphics error bars represent mean \pm SD from three independent experiments. * $p < 0.05$, ** $p < 0.01$, *** $p < 0.0001$. The following statistic were applied: for graphs in D two-way ANOVA with Tukey's post hoc test was applied and for graphs in G unpaired t test was applied. See also Figure S1.

676 **Figure 2. Proteomic analyses of sEVs secreted by cells with extra centrosomes support their endocytic origin.** (A) Experimental flowchart. (B) Venn diagram comparing the sEVs proteomes of SEC fractions 7, 8 and 9. (C) Venn diagram comparing the depicting the sEVs proteome of SEC fractions 7, 8 and 9 with the Vesiclepedia database. (D) Dotplot representation of the enrichment analyses

680 performed for the common proteins in all SEC fractions. Only proteins that were identified in both forward and reverse labelling experiments were considered for this analysis. See also Figure S2 and Tables S1-S3.

684 **Figure 3. ROS promote lysosome dysfunction and sEVs secretion in cells with extra centrosomes. (A)**
Schematic representation of intraluminal vesicle formation (ILVs) and multivesicular bodies (MVBs)
fate and how ROS could affect this process. (B) Levels of intracellular ROS quantified by the ratio of
GSH/GSSG in Patu-S.iPLK4 and HPAF-II.iPLK4 cell lines. Decrease in the GSH/GSSG ratio indicates
688 higher ROS levels. 5 mM of NAC and 100 μ M H₂O₂ was used. (C) Representative confocal images of
cells stained with Magic red (magenta), as a proxy for lysosome function, and for DNA (cyan). Scale
bar, 10 μ m. (D) Quantification of intracellular Magic red fluorescence intensity normalized for cell area
in Patu-S.iPLK4 cells. AU, arbitrary units. 5 mM of NAC and 100 μ M H₂O₂ was used. $n_{(-DOX)}=158$,
692 $n_{(+DOX)}=189$, $n_{(+DOX+NAC)}=221$ and $n_{(-DOX+H2O2)}=175$. (E) Quantification of secreted sEVs and lEVs in Patu-
S.iPLK4 and HPAF-II.iPLK4 cell lines. For all graphics error bars represent mean +/- SD from three
independent experiments. * $p < 0.05$, ** $p < 0.01$, *** $p < 0.001$, **** $p < 0.0001$, n.s. = not significant
($p > 0.05$). The following statistic were applied: for graphs in B one-way ANOVA with Tukey's post hoc
696 test, for D one-way ANOVA with a Kruskal-Wallis post hoc test and for E two-way ANOVA with Tukey's
post hoc test. See also Figure S3.

Figure 4. Centrosome amplification decreases lysosome-MVBs co-localization in a ROS-dependent
700 **manner. (A)** Representative confocal images of cells stained for acidic lysosomes (Lyotracker,
magenta), late endosomes/MVBs (anti-LBPA, green) and DNA (grey). Insets show higher magnification
of lysotracker and LBPA-labelled vesicles. Scale bar, 10 μ m. (B) Quantification of the number of
lysotracker-labelled lysosomes per cell. 5 mM of NAC and 100 μ M H₂O₂ was used. $n_{(-DOX)}=166$,
704 $n_{(+DOX)}=182$, $n_{(+DOX+NAC)}=245$ and $n_{(-DOX+H2O2)}=187$. (C) Quantification of LBPA-labelled late
endosomes/MVBs per cell. 5 mM of NAC and 100 μ M H₂O₂ was used. $n_{(-DOX)}=88$, $n_{(+DOX)}=102$,
 $n_{(+DOX+NAC)}=129$ and $n_{(-DOX+H2O2)}=99$. (D) Quantification of the percentage of lysotracker and LBPA-
labelled intracellular vesicles co-localization. 5 mM of NAC and 100 μ M H₂O₂ was used. $n_{(-DOX)}=86$,
708 $n_{(+DOX)}=102$, $n_{(+DOX+NAC)}=129$ and $n_{(-DOX+H2O2)}=98$. For all graphics error bars represent mean +/- SD from

three independent experiments. **** $p < 0.0001$, n.s. = not significant ($p > 0.05$). For all graphs a one-way ANOVA with a Kruskal-Wallis post hoc test was applied. See also Figure S4.

712 **Figure 5. sEVs secreted by PDAC cells with amplified centrosomes activate pancreatic stellate cells.**

(A) Experimental flowchart. (B) Representative confocal image of PSCs incubated with sEVs. Cells were stained for f-actin (phalloidin, grey) and DNA (cyan). Isolated sEVs were labelled with Bodipy (green). Scale bar = 10 μ m. (C) Representative confocal images of PSCs stained for α -SMA (green) and DNA (cyan). Scale bar, 10 μ m. (D) Quantification of the percentage of PSCs activation upon treatment with sEVs collected by UC from Patu-S.iPLK4 (left) and HPAF-II.iPLK4 (right), with (+DOX) and without (-DOX) extra centrosomes. Patu-S.iPLK4 isolated sEV: PSCs $n_{(-DOX\ sEVs)}=398$, $n_{(+DOX\ sEVs)}=373$, and $n_{(ctr)}=475$. HPAF-II.iPLK4 isolated sEV: PSCs $n_{(-DOX\ sEVs)}=914$, $n_{(+DOX\ sEVs)}=1057$, and $n_{(ctr)}=718$. (E) Quantification of the percentage of PSCs activation upon treatment with sEVs collected by SEC from Patu-S.iPLK4 (left) and HPAF-II.iPLK4 (right), with (+DOX) and without (-DOX) extra centrosomes. Patu-S.iPLK4 isolated sEV: PSCs $n_{(-DOX\ sEVs\ SEC7)}=161$, $n_{(+DOX\ sEVs\ SEC7)}=154$, PSCs $n_{(-DOX\ sEVs\ SEC8)}=490$, $n_{(+DOX\ sEVs\ SEC8)}=387$, PSCs $n_{(-DOX\ sEVs\ SEC9)}=463$, $n_{(+DOX\ sEVs\ SEC7)}=454$. HPAF-II.iPLK4 isolated sEV: PSCs $n_{(-DOX\ sEVs\ SEC7)}=499$, $n_{(+DOX\ sEVs\ SEC7)}=410$, PSCs $n_{(-DOX\ sEVs\ SEC8)}=541$, $n_{(+DOX\ sEVs\ SEC8)}=713$, PSCs $n_{(-DOX\ sEVs\ SEC9)}=1035$, $n_{(+DOX\ sEVs\ SEC7)}=914$. For all graphics error bars represent mean +/- SD from three independent experiments. *** $p < 0.001$, **** $p < 0.0001$, n.s. = not significant ($p > 0.05$). For all graphs were analyzed using by two-way ANOVA with Tukey's post hoc test. See also Figure S5.

728

Figure 6. sEVs secreted by cells with extra centrosomes can promote PDAC invasion. (A) Experimental

flowchart. (B) Representative brightfield images of heterotypic spheroids. Black arrows: invasive protrusions. Scale bar, 100 μ m. (C) Quantification of the percentage of invasion in 3D spheroids. 5 ng/ml TGF- β was used as positive control. Spheroids $n_{(+PSCs)}=40$, $n_{(+PSCs\ TGF-\beta)}=34$, $n_{(+PSCs\ -DOX\ sEVs)}=31$ and $n_{(+PSCs\ +DOX\ sEVs)}=31$. (D) Confocal images of spheroids composed of cancer cells (expressing H₂B-RFP; magenta) and PSCs (expressing H₂B-GFP; green). Scale bar, 100 μ m. Inset depicts higher

magnification of invasive protrusion. Scale bar, 20 μm . For all graphics error bars represent mean +/-
736 SD from three independent experiments. **** $p < 0.0001$, n.s. = not significant ($p > 0.05$). Graph was
analyzed using one-way ANOVA with a Kruskal-Wallis post hoc test.

Figure 7. Schematic representation of working model. Increased ROS levels in cells with extra
740 centrosomes compromises lysosomal function. We propose that this changes MVBs fate towards
fusing with the plasma membrane and secretion of sEVs. sEVs secreted by cancer cells with extra
centrosomes are functionally distinct and can induce PSCs activation to promote cell invasion.

744

748

752

756

760

References

1. Chan, J.Y. (2011). A clinical overview of centrosome amplification in human cancers. *Int J Biol Sci* **7**, 1122-1144.
- 764 2. Zyss, D., and Gergely, F. (2009). Centrosome function in cancer: guilty or innocent? *Trends Cell Biol* **19**, 334-346.
3. Basto, R., Brunk, K., Vinadogrova, T., Peel, N., Franz, A., Khodjakov, A., and Raff, J.W. (2008). Centrosome amplification can initiate tumorigenesis in flies. *Cell* **133**, 1032-1042.
- 768 4. Levine, M.S., Bakker, B., Boeckx, B., Moyett, J., Lu, J., Vitre, B., Spierings, D.C., Lansdorp, P.M., Cleveland, D.W., Lambrechts, D., et al. (2017). Centrosome Amplification Is Sufficient to Promote Spontaneous Tumorigenesis in Mammals. *Developmental cell* **40**, 313-322 e315.
- 772 5. Coelho, P.A., Bury, L., Shahbazi, M.N., Liakath-Ali, K., Tate, P.H., Wormald, S., Hindley, C.J., Huch, M., Archer, J., Skarnes, W.C., et al. (2015). Over-expression of Plk4 induces centrosome amplification, loss of primary cilia and associated tissue hyperplasia in the mouse. *Open Biol* **5**, 150209.
- 776 6. Sercin, O., Larsimont, J.C., Karambelas, A.E., Marthiens, V., Moers, V., Boeckx, B., Le Mercier, M., Lambrechts, D., Basto, R., and Blanpain, C. (2016). Transient PLK4 overexpression accelerates tumorigenesis in p53-deficient epidermis. *Nat Cell Biol* **18**, 100-110.
7. Ganem, N.J., Godinho, S.A., and Pellman, D. (2009). A mechanism linking extra centrosomes to chromosomal instability. *Nature* **460**, 278-282.
- 780 8. Godinho, S.A., and Pellman, D. (2014). Causes and consequences of centrosome abnormalities in cancer. *Philosophical transactions of the Royal Society of London. Series B, Biological sciences* **369**.
- 784 9. Silkworth, W.T., Nardi, I.K., Scholl, L.M., and Cimini, D. (2009). Multipolar spindle pole coalescence is a major source of kinetochore mis-attachment and chromosome mis-segregation in cancer cells. *PLoS One* **4**, e6564.
- 788 10. Arnandis, T., Monteiro, P., Adams, S.D., Bridgeman, V.L., Rajeeve, V., Gadaleta, E., Marzec, J., Chelala, C., Malanchi, I., Cutillas, P.R., et al. (2018). Oxidative Stress in Cells with Extra Centrosomes Drives Non-Cell-Autonomous Invasion. *Developmental cell* **47**, 409-424 e409.
11. Place, A.E., Jin Huh, S., and Polyak, K. (2011). The microenvironment in breast cancer progression: biology and implications for treatment. *Breast Cancer Res* **13**, 227.
- 792 12. Quail, D.F., and Joyce, J.A. (2013). Microenvironmental regulation of tumor progression and metastasis. *Nat Med* **19**, 1423-1437.
13. van Niel, G., D'Angelo, G., and Raposo, G. (2018). Shedding light on the cell biology of extracellular vesicles. *Nat Rev Mol Cell Biol* **19**, 213-228.
- 796 14. Costa-Silva, B., Aiello, N.M., Ocean, A.J., Singh, S., Zhang, H., Thakur, B.K., Becker, A., Hoshino, A., Mark, M.T., Molina, H., et al. (2015). Pancreatic cancer exosomes initiate pre-metastatic niche formation in the liver. *Nat Cell Biol* **17**, 816-826.
- 800 15. Hurwitz, S.N., Rider, M.A., Bundy, J.L., Liu, X., Singh, R.K., and Meckes, D.G., Jr. (2016). Proteomic profiling of NCI-60 extracellular vesicles uncovers common protein cargo and cancer type-specific biomarkers. *Oncotarget* **7**, 86999-87015.
- 804 16. Xu, R., Rai, A., Chen, M., Suwakulsiri, W., Greening, D.W., and Simpson, R.J. (2018). Extracellular vesicles in cancer - implications for future improvements in cancer care. *Nat Rev Clin Oncol* **15**, 617-638.
- 808 17. Webber, J., Steadman, R., Mason, M.D., Tabi, Z., and Clayton, A. (2010). Cancer exosomes trigger fibroblast to myofibroblast differentiation. *Cancer Res* **70**, 9621-9630.
18. Webber, J.P., Spary, L.K., Sanders, A.J., Chowdhury, R., Jiang, W.G., Steadman, R., Wymant, J., Jones, A.T., Kynaston, H., Mason, M.D., et al. (2015). Differentiation of tumour-promoting stromal myofibroblasts by cancer exosomes. *Oncogene* **34**, 290-302.

19. Ringuette Goulet, C., Bernard, G., Tremblay, S., Chabaud, S., Bolduc, S., and Pouliot, F. (2018). Exosomes Induce Fibroblast Differentiation into Cancer-Associated Fibroblasts through TGFbeta Signaling. *Mol Cancer Res* *16*, 1196-1204.
- 812 20. Mohammadi, H., and Sahai, E. (2018). Mechanisms and impact of altered tumour mechanics. *Nat Cell Biol* *20*, 766-774.
21. Fujita, H., Ohuchida, K., Mizumoto, K., Nakata, K., Yu, J., Kayashima, T., Cui, L., Manabe, T., Ohtsuka, T., and Tanaka, M. (2010). alpha-Smooth Muscle Actin Expressing Stroma Promotes an Aggressive Tumor Biology in Pancreatic Ductal Adenocarcinoma. *Pancreas* *39*, 1254-1262.
- 816 22. McCarroll, J.A., Naim, S., Sharbeen, G., Russia, N., Lee, J., Kavallaris, M., Goldstein, D., and Phillips, P.A. (2014). Role of pancreatic stellate cells in chemoresistance in pancreatic cancer. *Frontiers in physiology* *5*, 141.
- 820 23. Kadaba, R., Birke, H., Wang, J., Hooper, S., Andl, C.D., Di Maggio, F., Soyulu, E., Ghallab, M., Bor, D., Froeling, F.E., et al. (2013). Imbalance of desmoplastic stromal cell numbers drives aggressive cancer processes. *J Pathol* *230*, 107-117.
24. Zhang, Y.F., Zhou, Y.Z., Zhang, B., Huang, S.F., Li, P.P., He, X.M., Cao, G.D., Kang, M.X., Dong, X., and Wu, Y.L. (2019). Pancreatic cancer-derived exosomes promoted pancreatic stellate cells recruitment by pancreatic cancer. *J Cancer* *10*, 4397-4407.
- 824 25. Headland, S.E., Jones, H.R., D'Sa, A.S., Perretti, M., and Norling, L.V. (2014). Cutting-edge analysis of extracellular microparticles using ImageStream(X) imaging flow cytometry. *Sci Rep* *4*, 5237.
- 828 26. Godinho, S.A., Picone, R., Burute, M., Dagher, R., Su, Y., Leung, C.T., Polyak, K., Brugge, J.S., Thery, M., and Pellman, D. (2014). Oncogene-like induction of cellular invasion from centrosome amplification. *Nature* *510*, 167-171.
- 832 27. Kowal, J., Tkach, M., and Thery, C. (2014). Biogenesis and secretion of exosomes. *Curr Opin Cell Biol* *29*, 116-125.
28. Colombo, M., Moita, C., van Niel, G., Kowal, J., Vigneron, J., Benaroch, P., Manel, N., Moita, L.F., Thery, C., and Raposo, G. (2013). Analysis of ESCRT functions in exosome biogenesis, composition and secretion highlights the heterogeneity of extracellular vesicles. *J Cell Sci* *126*, 5553-5565.
- 836 29. Mardakheh, F.K., Sailem, H.Z., Kumper, S., Tape, C.J., McCully, R.R., Paul, A., Anjomani-Virmouni, S., Jorgensen, C., Poulogiannis, G., Marshall, C.J., et al. (2016). Proteomics profiling of interactome dynamics by colocalisation analysis (COLA). *Mol Biosyst* *13*, 92-105.
- 840 30. Boing, A.N., van der Pol, E., Grootemaat, A.E., Coumans, F.A., Sturk, A., and Nieuwland, R. (2014). Single-step isolation of extracellular vesicles by size-exclusion chromatography. *J Extracell Vesicles* *3*.
- 844 31. Muller, L., Hong, C.S., Stolz, D.B., Watkins, S.C., and Whiteside, T.L. (2014). Isolation of biologically-active exosomes from human plasma. *J Immunol Methods* *411*, 55-65.
32. Kalra, H., Simpson, R.J., Ji, H., Aikawa, E., Altevogt, P., Askenase, P., Bond, V.C., Borrás, F.E., Breakefield, X., Budnik, V., et al. (2012). Vesiclepedia: a compendium for extracellular vesicles with continuous community annotation. *PLoS Biol* *10*, e1001450.
- 848 33. Harding, C., Heuser, J., and Stahl, P. (1983). Receptor-mediated endocytosis of transferrin and recycling of the transferrin receptor in rat reticulocytes. *The Journal of cell biology* *97*, 329-339.
- 852 34. Alvarez-Erviti, L., Seow, Y., Schapira, A.H., Gardiner, C., Sargent, I.L., Wood, M.J., and Cooper, J.M. (2011). Lysosomal dysfunction increases exosome-mediated alpha-synuclein release and transmission. *Neurobiol Dis* *42*, 360-367.
35. Latifkar, A., Ling, L., Hingorani, A., Johansen, E., Clement, A., Zhang, X., Hartman, J., Fischbach, C., Lin, H., Cerione, R.A., et al. (2019). Loss of Sirtuin 1 Alters the Secretome of Breast Cancer Cells by Impairing Lysosomal Integrity. *Developmental cell* *49*, 393-408 e397.
- 856 36. Miao, Y., Li, G., Zhang, X., Xu, H., and Abraham, S.N. (2015). A TRP Channel Senses Lysosome Neutralization by Pathogens to Trigger Their Expulsion. *Cell* *161*, 1306-1319.

- 860 37. Aits, S., and Jaattela, M. (2013). Lysosomal cell death at a glance. *J Cell Sci* 126, 1905-1912.
38. Nilsson, E., Ghassemifar, R., and Brunk, U.T. (1997). Lysosomal heterogeneity between and within cells with respect to resistance against oxidative stress. *Histochem J* 29, 857-865.
39. Leung-Toung, R., Li, W., Tam, T.F., and Karimian, K. (2002). Thiol-dependent enzymes and their inhibitors: a review. *Curr Med Chem* 9, 979-1002.
- 864 40. Yoshimori, T., Yamamoto, A., Moriyama, Y., Futai, M., and Tashiro, Y. (1991). Bafilomycin A1, a specific inhibitor of vacuolar-type H(+)-ATPase, inhibits acidification and protein degradation in lysosomes of cultured cells. *J Biol Chem* 266, 17707-17712.
- 868 41. Savina, A., Furlan, M., Vidal, M., and Colombo, M.I. (2003). Exosome release is regulated by a calcium-dependent mechanism in K562 cells. *J Biol Chem* 278, 20083-20090.
42. Kobayashi, T., Stang, E., Fang, K.S., de Moerloose, P., Parton, R.G., and Gruenberg, J. (1998). A lipid associated with the antiphospholipid syndrome regulates endosome structure and function. *Nature* 392, 193-197.
- 872 43. Zhitomirsky, B., Farber, H., and Assaraf, Y.G. (2018). LysoTracker and MitoTracker Red are transport substrates of P-glycoprotein: implications for anticancer drug design evading multidrug resistance. *J Cell Mol Med* 22, 2131-2141.
- 876 44. Masamune, A., Yoshida, N., Hamada, S., Takikawa, T., Nabeshima, T., and Shimosegawa, T. (2018). Exosomes derived from pancreatic cancer cells induce activation and profibrogenic activities in pancreatic stellate cells. *Biochem Biophys Res Commun* 495, 71-77.
45. Erkan, M., Adler, G., Apte, M.V., Bachem, M.G., Buchholz, M., Detlefsen, S., Esposito, I., Friess, H., Gress, T.M., Habisch, H.J., et al. (2012). StellaTUM: current consensus and discussion on pancreatic stellate cell research. *Gut* 61, 172-178.
- 880 46. Apte, M.V., Park, S., Phillips, P.A., Santucci, N., Goldstein, D., Kumar, R.K., Ramm, G.A., Buchler, M., Friess, H., McCarroll, J.A., et al. (2004). Desmoplastic reaction in pancreatic cancer: role of pancreatic stellate cells. *Pancreas* 29, 179-187.
- 884 47. Sahai, E., Astsaturov, I., Cukierman, E., DeNardo, D.G., Egeblad, M., Evans, R.M., Fearon, D., Greten, F.R., Hingorani, S.R., Hunter, T., et al. (2020). A framework for advancing our understanding of cancer-associated fibroblasts. *Nat Rev Cancer* 20, 174-186.
- 888 48. Labernadie, A., Kato, T., Brugues, A., Serra-Picamal, X., Derzsi, S., Arwert, E., Weston, A., Gonzalez-Tarrago, V., Elosegui-Artola, A., Albertazzi, L., et al. (2017). A mechanically active heterotypic E-cadherin/N-cadherin adhesion enables fibroblasts to drive cancer cell invasion. *Nat Cell Biol* 19, 224-237.
- 892 49. Shin, H.R., and Zoncu, R. (2020). The Lysosome at the Intersection of Cellular Growth and Destruction. *Developmental cell* 54, 226-238.
50. Denu, R.A., Kaur, G., Sass, M.M., Lakkaraju, A., and Burkard, M.E. (2020). Centrosome Amplification in Cancer Disrupts Autophagy and Sensitizes to Autophagy Inhibition. *Mol Cancer Res* 18, 33-45.
- 896 51. Willms, E., Johansson, H.J., Mager, I., Lee, Y., Blomberg, K.E., Sadik, M., Alaarg, A., Smith, C.I., Lehtio, J., El Andaloussi, S., et al. (2016). Cells release subpopulations of exosomes with distinct molecular and biological properties. *Sci Rep* 6, 22519.
- 900 52. Tauro, B.J., Greening, D.W., Mathias, R.A., Mathivanan, S., Ji, H., and Simpson, R.J. (2013). Two distinct populations of exosomes are released from LIM1863 colon carcinoma cell-derived organoids. *Mol Cell Proteomics* 12, 587-598.
53. McKelvey, K.J., Powell, K.L., Ashton, A.W., Morris, J.M., and McCracken, S.A. (2015). Exosomes: Mechanisms of Uptake. *J Circ Biomark* 4, 7.
- 904 54. Buzas, E.I., Toth, E.A., Sodar, B.W., and Szabo-Taylor, K.E. (2018). Molecular interactions at the surface of extracellular vesicles. *Semin Immunopathol* 40, 453-464.
55. Willms, E., Cabanas, C., Mager, I., Wood, M.J.A., and Vader, P. (2018). Extracellular Vesicle Heterogeneity: Subpopulations, Isolation Techniques, and Diverse Functions in Cancer Progression. *Front Immunol* 9, 738.
- 908

56. Laulagnier, K., Javalet, C., Hemming, F.J., Chivet, M., Lachenal, G., Blot, B., Chatellard, C., and Sadoul, R. (2018). Amyloid precursor protein products concentrate in a subset of exosomes specifically endocytosed by neurons. *Cell Mol Life Sci* **75**, 757-773.
- 912 57. O'Neill, C.P., Gilligan, K.E., and Dwyer, R.M. (2019). Role of Extracellular Vesicles (EVs) in Cell Stress Response and Resistance to Cancer Therapy. *Cancers (Basel)* **11**.
58. Eldh, M., Ekstrom, K., Valadi, H., Sjostrand, M., Olsson, B., Jernas, M., and Lotvall, J. (2010). Exosomes communicate protective messages during oxidative stress; possible role of exosomal shuttle RNA. *PLoS One* **5**, e15353.
- 916 59. Li, N.F., Kocher, H.M., Salako, M.A., Obermueller, E., Sandle, J., and Balkwill, F. (2009). A novel function of colony-stimulating factor 1 receptor in hTERT immortalization of human epithelial cells. *Oncogene* **28**, 773-780.
- 920 60. Campeau, E., Ruhl, V.E., Rodier, F., Smith, C.L., Rahmberg, B.L., Fuss, J.O., Campisi, J., Yaswen, P., Cooper, P.K., and Kaufman, P.D. (2009). A versatile viral system for expression and depletion of proteins in mammalian cells. *PLoS One* **4**, e6529.
- 924 61. Schneider, C.A., Rasband, W.S., and Eliceiri, K.W. (2012). NIH Image to ImageJ: 25 years of image analysis. *Nat Methods* **9**, 671-675.
62. Lo Cicero, A., Delevoye, C., Gilles-Marsens, F., Loew, D., Dingli, F., Guere, C., Andre, N., Vie, K., van Niel, G., and Raposo, G. (2015). Exosomes released by keratinocytes modulate melanocyte pigmentation. *Nat Commun* **6**, 7506.
- 928 63. Mardakheh, F.K., Paul, A., Kumper, S., Sadok, A., Paterson, H., McCarthy, A., Yuan, Y., and Marshall, C.J. (2015). Global Analysis of mRNA, Translation, and Protein Localization: Local Translation Is a Key Regulator of Cell Protrusions. *Developmental cell* **35**, 344-357.
- 932 64. Rappsilber, J., Mann, M., and Ishihama, Y. (2007). Protocol for micro-purification, enrichment, pre-fractionation and storage of peptides for proteomics using StageTips. *Nat Protoc* **2**, 1896-1906.
- 936 65. Tyanova, S., Temu, T., and Cox, J. (2016). The MaxQuant computational platform for mass spectrometry-based shotgun proteomics. *Nat Protoc* **11**, 2301-2319.
66. Vizcaino, J.A., Deutsch, E.W., Wang, R., Csordas, A., Reisinger, F., Rios, D., Dianes, J.A., Sun, Z., Farrah, T., Bandeira, N., et al. (2014). ProteomeXchange provides globally coordinated proteomics data submission and dissemination. *Nat Biotechnol* **32**, 223-226.
- 940

Figure 1

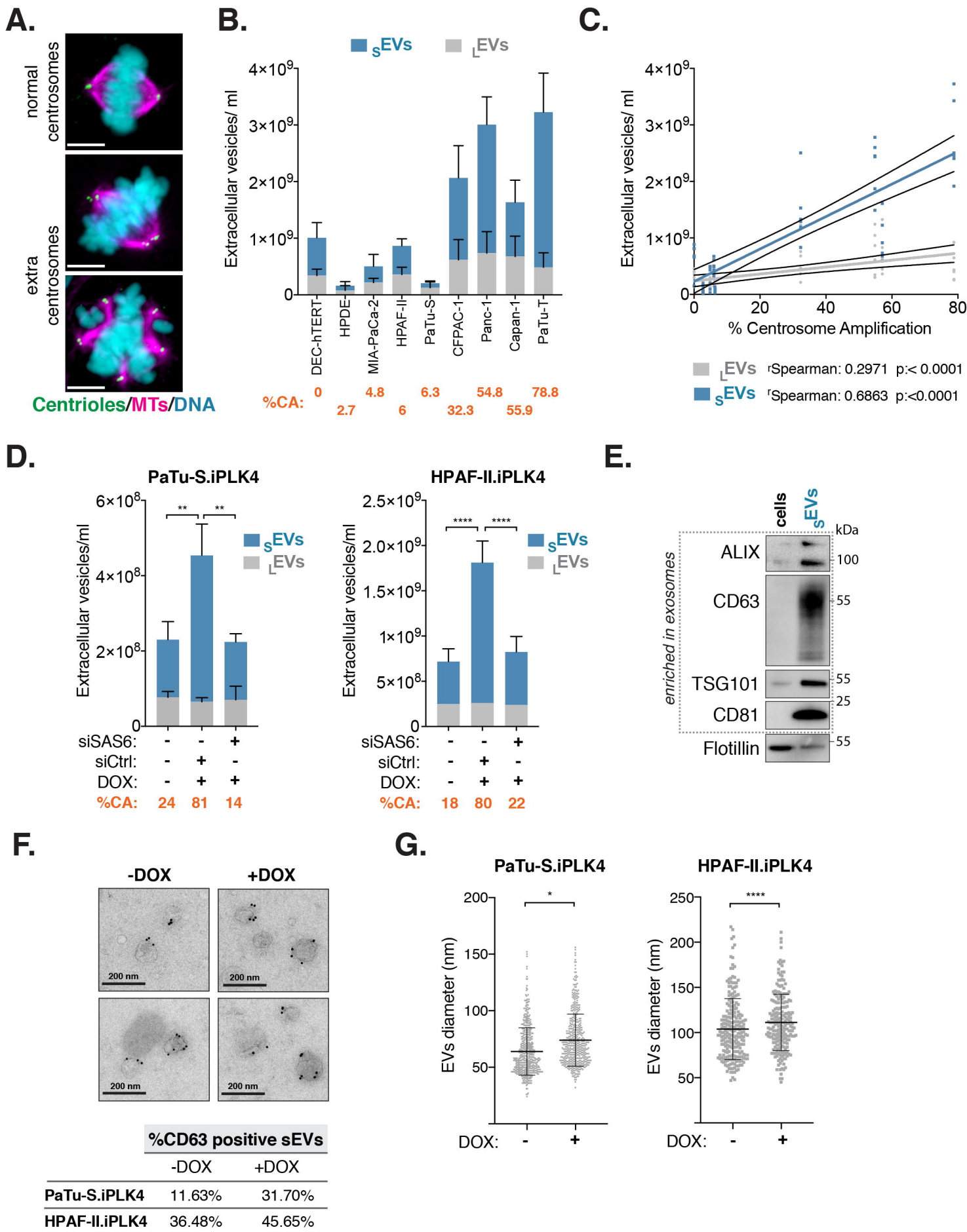
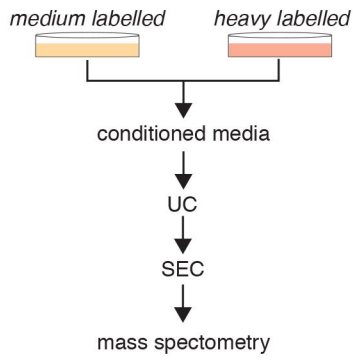
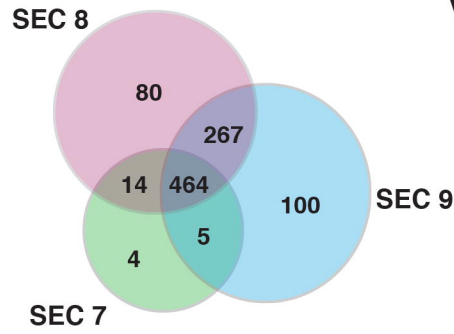


Figure 2

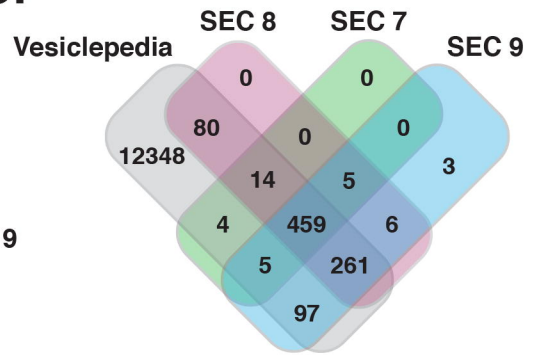
A.



B.



C.



D.

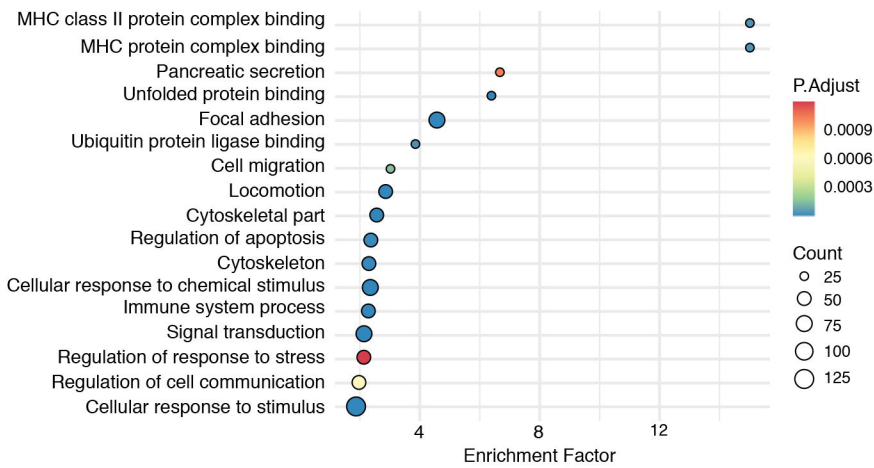
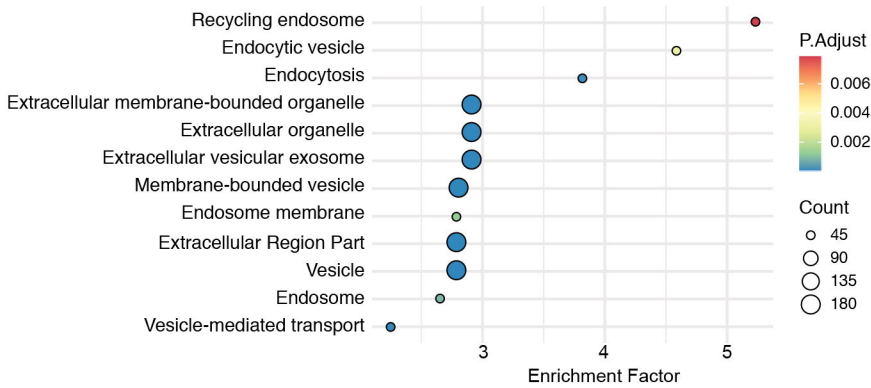


Figure 3

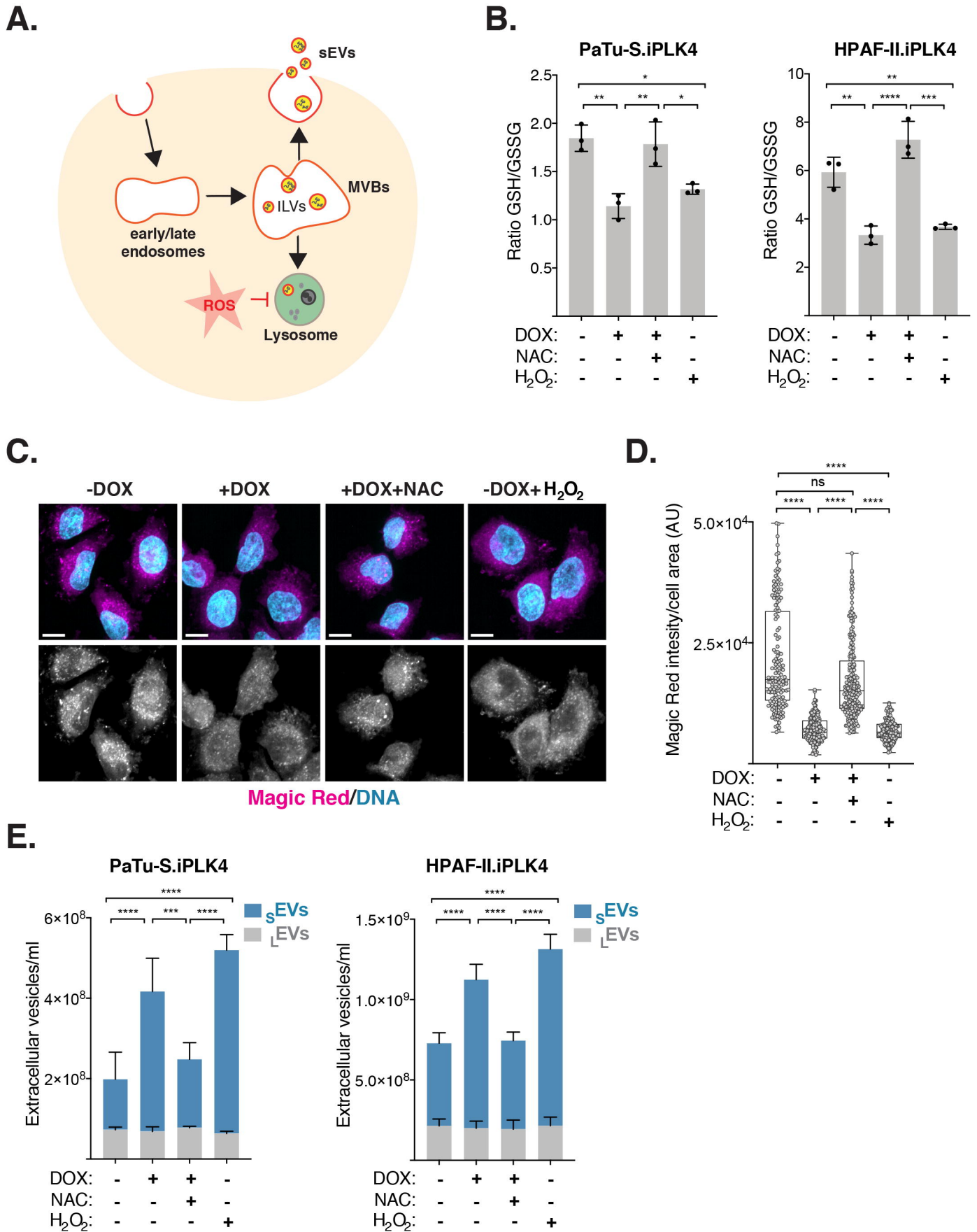


Figure 4

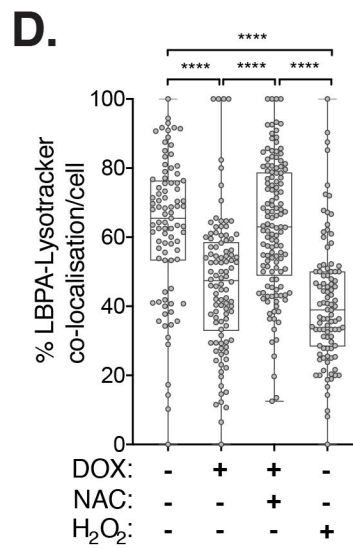
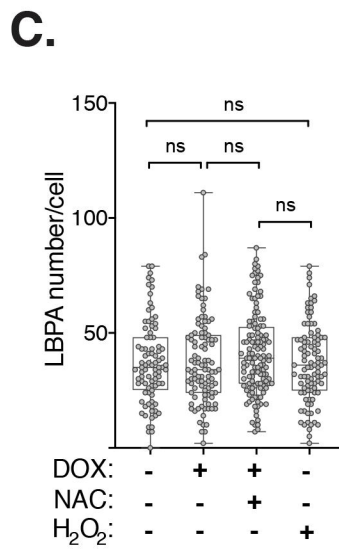
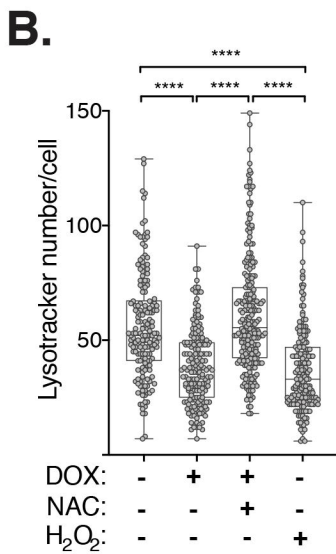
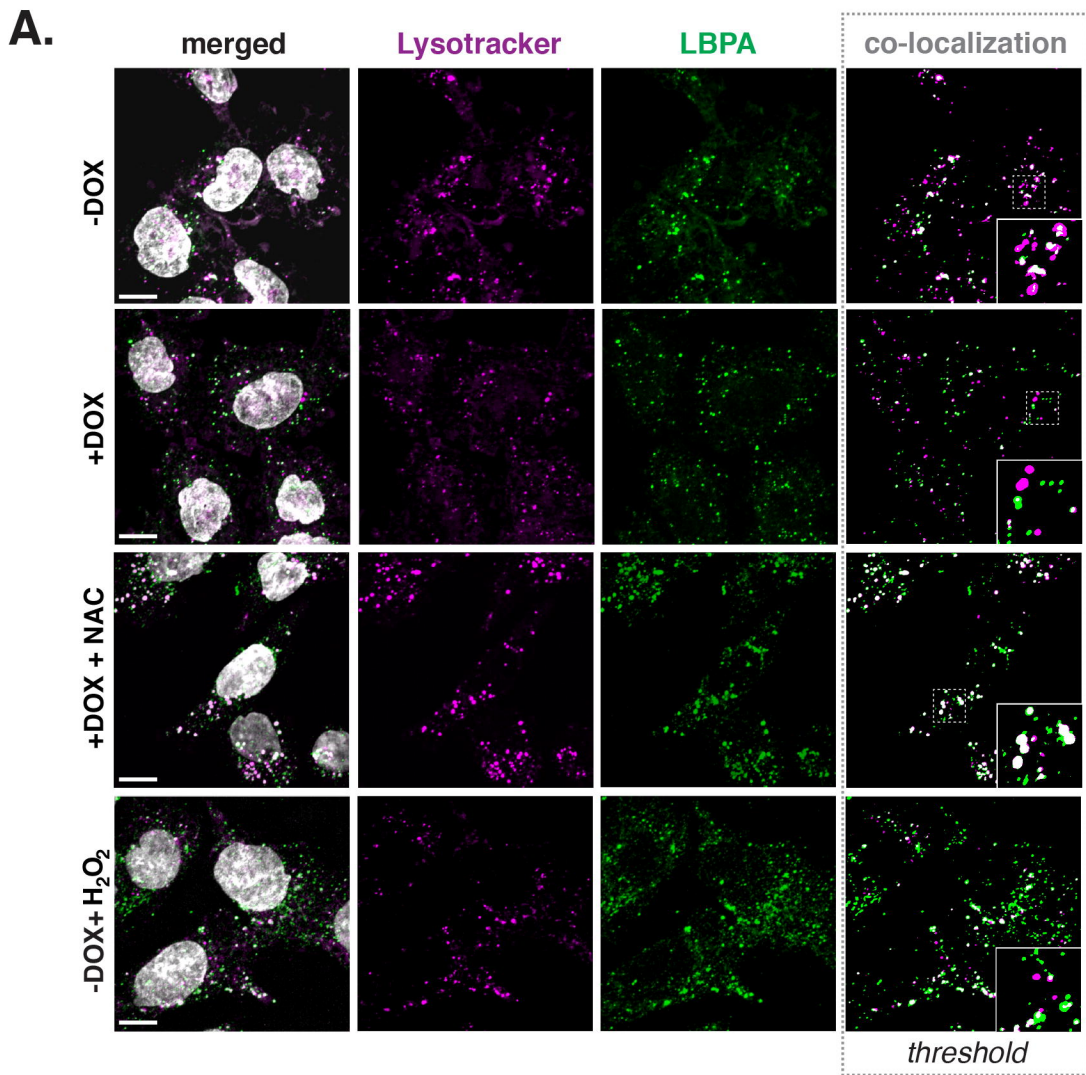
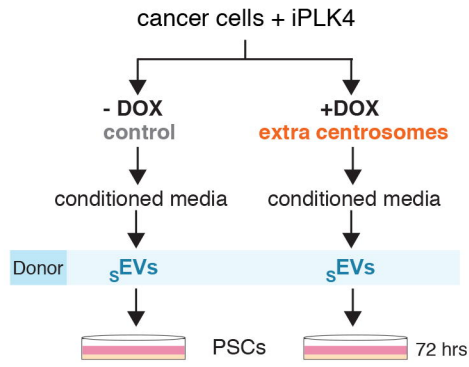
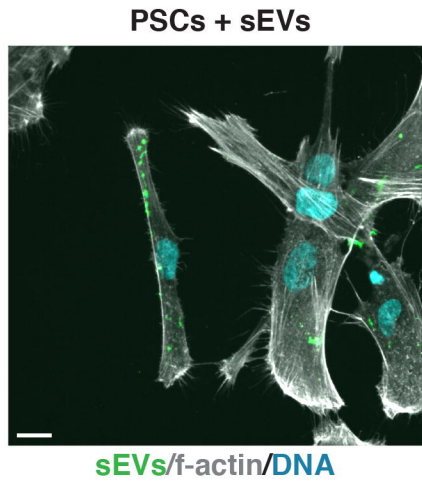


Figure 5

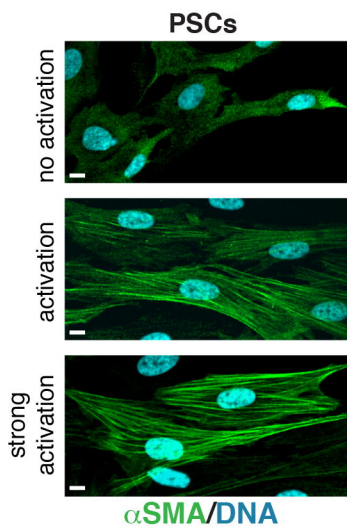
A.



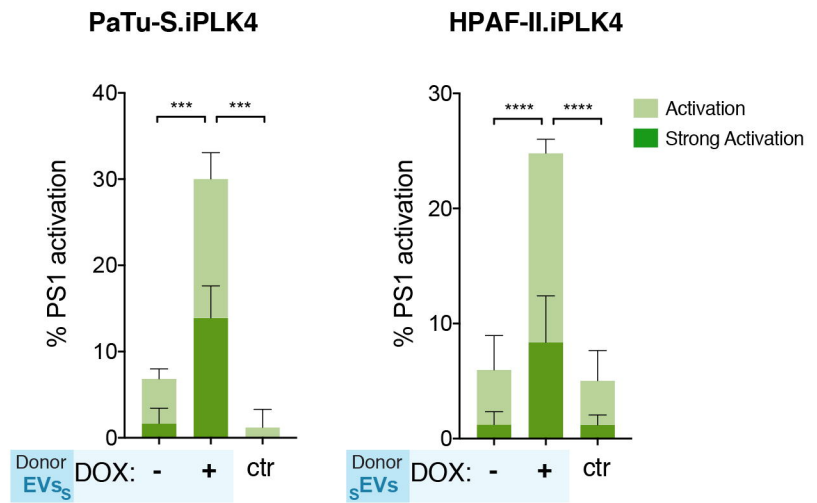
B.



C.



D.



E.

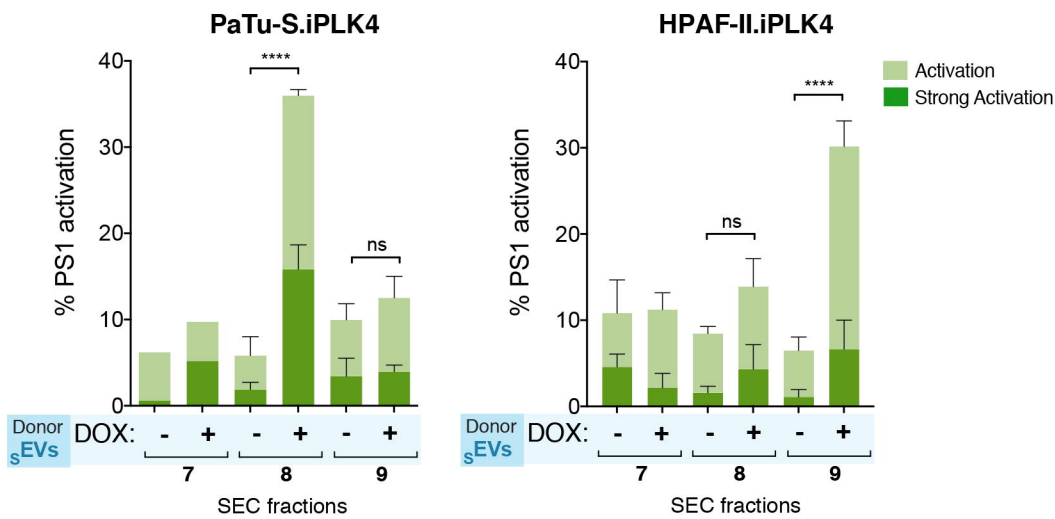


Figure 6

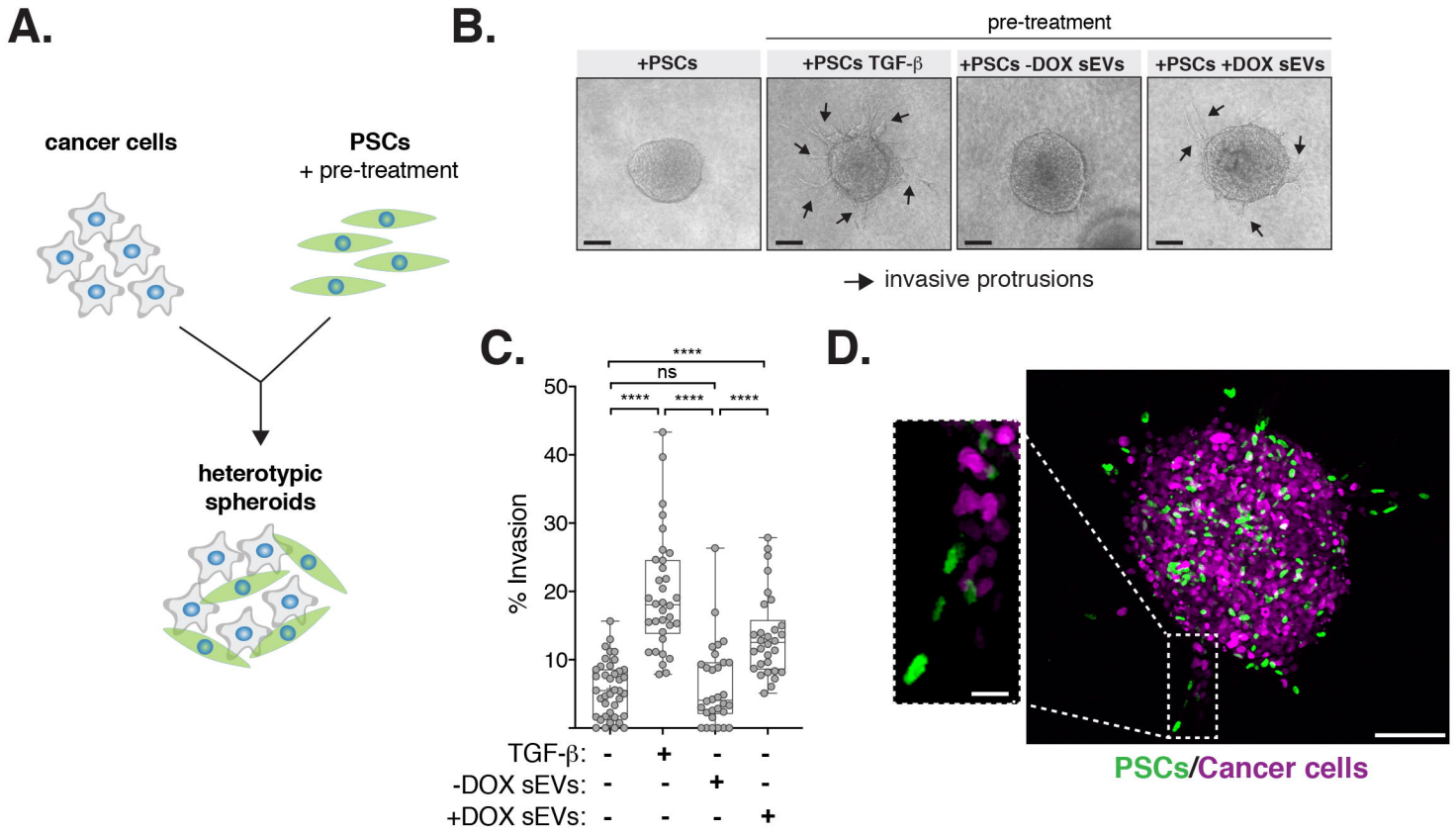


Figure 7

